Origin of improved tunability and loss in N_2 annealed barium strontium titanate films

Ali Mostaed[a, b*], Ioanna Bakaimi[c], Brian Hayden[c,d], Derek C. Sinclair[a] and Ian M. Reaney[a]

[a] Department of Materials Science and Engineering, University of Sheffield, Sheffield S1 3JD, UK
[b] now at Department of Materials, University of Oxford, Parks Road, Oxford OX1 3PH, UK
[c] School of Chemistry, The University of Southampton, Highfield, Southampton SO 171BJ, UK
[d] Ilika Technologies, Unit 10a The Quadrangle, Abbey Park Industrial Estate, Romsey, Hampshire SO51 9DL

Abstract

Barium strontium titanate (BSTO) thin-films were deposited on Pt(111) by high throughput evaporative physical vapour deposition (HT-ePVD) and then annealed at 650 °C for 30 min under N_2 atmosphere. Using advanced transmission electron microscopy, energy-dispersive x-ray spectroscopy (EDX) and electron energy loss spectroscopy (EELS), we directly show, that not only does N substitute for O in the BSTO lattice but that it also compensates for Ti^{3+} ions, suppressing conductivity, thereby reducing dielectric loss and enhancing dielectric tunability. However, this effect is negated near the film edge where we speculate that exposed Pt acts as a reservoir of adsorbed/absorbed O and alters the local N_2 concentration during annealing.

Keywords: Oxygen vacancies; high throughput physical vapour deposition; Dielectric tunability

* Corresponding author: ali.mostaed@materials.ox.ac.uk

I. Introduction

Thin film barium strontium titanate ($Ba_xSr_{1-x}TiO_3$), hereafter referred to as BSTO is a promising candidate for applications as tunable capacitors [1,2], tunable microwave devices [3,4] and microwave phase shifters [2,5]. Paraelectric BSTO thin films (~200 nm) have been shown to exhibit >50% dielectric tunability under dc bias (2–5 V) [2,6,7] but their relative permittivity (ε_r), dielectric loss and tunability depend on various factors. Previous studies have highlighted the effect of film thickness [8], grain size [9-11], grain boundary orientation [12], secondary amorphous phases [13], composition, stoichiometry, dopants [14,15], substrate residual stresses [3,16] and the formation of interfacial dead layers [17,18] on the dielectric loss, ε_r and tunability. Practically, BSTO thin films are optimized by tailoring their stoichiometry, composition, lateral grain size, and thickness during deposition and are often subjected to a suitable post-deposition [19] heat treatment to improve resistivity. The improvement in resistivity is attributed to modification of the film's defect chemistry but the role of point defects such as oxygen vacancies (V_O) and associated Ti^{3+} ions are rarely investigated by direct methods. Rather, their existence is implied from their potential contribution to the dielectric properties and conductivity [20,21].

High throughput evaporative physical vapour deposition (HT-ePVD) has been exploited to deposit $Ba_xSr_{1-x}TiO_3$ thin films on Pt coated substrates [22]. HT-ePVD is based on the evaporation of elemental sources employing wedge shutters to obtain a compositional spread that results in physical property changes across the film. Different dopants are incorporated onto the *A*- (Ba), *B*- (Ti) or simultaneously on the *A* and *B* sites [23,24] of the ABO_3 perovskite structure, resulting in ternary or quaternary solid solutions [25]. A plasma atom source is used to provide reactive oxygen co-deposited with metal atoms: This ensures oxygen stoichiometry during synthesis, at temperatures much lower than post annealing in molecular oxygen. In addition, large growth rates can be achieved resulting in relatively thick layers (250-300 nm) in <90 min.

Here we use scanning transmission electron microscopy (STEM) in conjunction with energy dispersive X-ray (EDX) spectroscopy and electron energy loss spectroscopy (EELS) to investigate the structure and chemistry of BSTO thin-films that have been subjected to a post-deposition heat treatment in N_2. We demonstrate through direct observation rather than inference that N is incorporated into the lattice which compensates for Ti^{3+} ions, suppresses conductivity and results in lower dielectric loss and enhanced dielectric tunability.

II. Experimental methods

$Ba_xSr_{1-x}TiO_3$ was deposited on Pt coated substrates ($Pt/TiO_2/SiO_2/Si$) using a high throughput modified Molecular Beam Epitaxy [22] system from DCA Instruments, as described elsewhere [23]. Elemental sources of Ba (Alfa Aesar: 99.9%) and Sr pieces (Alfa Aesar: 99%) were contained in Ta and PBN crucibles respectively and evaporated using Knudsen cells. Ti pellets (Testbourne 99.995%) were placed on a graphite crucible and evaporated using a 40 cc electron gun. An RF atom source of 545 W (HD25, Oxford Applied Research) produced atomic oxygen with a flow rate of 1.02 ml/min. Substrate temperature *in situ* was 640 °C. Films where post annealed in a tube furnace at 650 °C for 30 min under N_2 with a flow rate of 2.5 $Lmin^{-1}$.

Films thickness varied between 170-250 nm for a deposition time of 60 minutes. Scanning electron microscopy (SEM) was carried out using a Tesca Vega 3 equipped with an EDX detector XMax 50 (Oxford Instruments). A Bruker D8 x-ray diffractometer equipped with an Incoatec microsource Cu K_α and GADDS detector were used to map film composition and crystal structure.

For dielectric measurements, a 14×14 array of 290 μm diameter platinum top electrodes was deposited onto the film surface using RF sputtering. The dielectric loss and capacitance (C) of the thin films were measured at 1 kHz-100 kHz using an LCR bridge (Hewlett Packard 4284A) with an AC voltage of 100 mV. The dielectric permittivity (ε_r) and tunability n_r of the thin films were calculated using Eqs. (1) and (2):

$$\varepsilon_r = \frac{Cd}{\varepsilon_0 A}, \quad (1)$$

$$n_r = 100 \times \frac{\varepsilon_v - \varepsilon_0}{\varepsilon_0}, \quad (2)$$

where, ε_0, d, A and ε_v are the dielectric constant under zero electric field (8.854×10^{-12} Fm^{-1}), thickness of the BSTO film, conductive area of the electrodes and dielectric constant under a DC electric field, respectively.

Regions 1 and 2, marked by circles in Fig. 1(a), were chosen for TEM investigations as they exhibit quite different optical (i.e. colour) and dielectric properties while there were no significant difference in their cation composition (according to SEM-EDX results not shown here). Cross-sectional samples for TEM characterization were prepared by grinding and polishing to <40 μm, followed by ion milling to electron transparency using a GATAN precision Ar-ion polishing system II (PIPSII). Ion milling was carried using LN_2 cooling

initially at 5 keV followed by final milling at 1 keV. A JEOL JEM F200 transmission electron microscope operating at 200 keV was used to acquire TEM data from the samples.

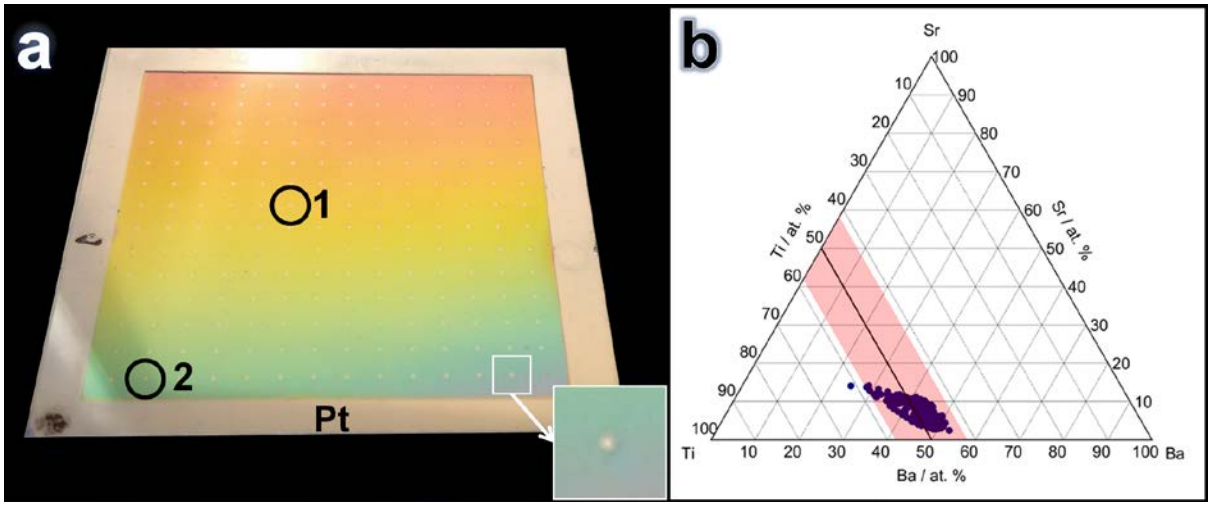

Figure 1: (a) $Ba_xSr_{1-x}TiO_3$ film with Pt electrodes shown as circular dots on the surface of the film. The color differentiation corresponds to the compositional gradient. The two points indicated on the film were subjected to further analysis using advanced TEM. (b) Ternary plot of Ba, Sr and Ti obtained by EDX analysis. The black line represents the $SrTiO_3$–$BaTiO_3$ pseudobinary line. The shaded area shows the limits of composition where the perovskite structure is retained.

III. Results

3.1 Composition and Structure

High throughput EDX analysis was carried out to determine the composition of the fabricated samples. Sr, Ba and Ti concentrations varied from 4-14 at.%, 30-50 at.% and 45-55 at.%, respectively, across the film, as illustrated in Fig. 1(b). High throughput X-ray diffraction confirmed the film crystal structure and phase assemblage. Fig. 2(a) shows the X-ray patterns obtained from regions 1 and 2 displayed in Fig. 1(a). All peaks indexed according to a single perovskite phase. The distribution of relative intensities in the XRD pattern suggest that the films favour a 100 orientation but with some random orientation as evidenced by the strong 101 peak (100% peak in powder XRD from BSTO ceramics, e.g. PDF card 01-082-8710). The lattice parameters and peak positions from regions 1 and 2 were consistent with compositions rich in Ba and matched best with $Ba_{0.85}Sr_{0.15}TiO_3$ (PDF card 01-082-8710). We note that the peak matching gives only a qualitative indication of film composition since the ICDD database contains only a limited number of entries for different Ba/Sr ratios in BSTO. Moreover, none of these references are from thin films which suffer from peak shifting due to strain, arising from thermal expansion mismatch between substrate and film on cooling. The peaks at 39.8

and 46 are attributed to the (111) and (200) of the Pt bottom electrode (see inset of lower XRD pattern).

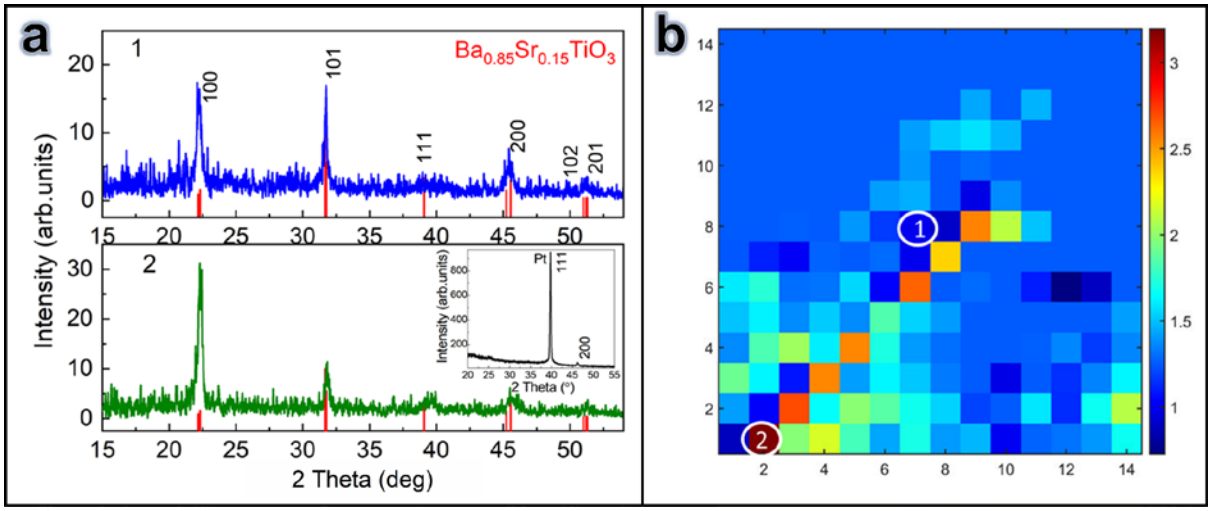

Figure2 (a): X-ray diffraction patterns obtained from Regions 1 and 2 illustrated in Fig. 1(a). The vertical red tick marks correspond to the $Ba_{0.85}Sr_{0.15}TiO_3$ (PDF card 01-082-8710) indicating a match with this perovskite phase. The inset figure on the bottom right shows an X-ray diffraction pattern obtained from the SSTOP substrate, which shows the 111 and 200 reflections of Pt at 39.8 and 46 degrees, respectively. (b): Map of the 100/101 intensity ratio across the film.

One difference between regions 1 and 2 is in the relative intensity of the peaks at 22 (100) and 31 (101) deg. In Region 1 (blue pattern), the intensity of the 100 peak at 22 deg (I_{p22}) is similar to the intensity of the 101 peak at 31 deg (I_{p31}). In Region 2 the peak at 22 deg has a higher intensity than the 101 peak with I_{p22}/I_{p31} about 3 times that of region 1 Fig. 2(b). Although there have been studies that correlate optimum dielectric properties with a preferred orientation [26-28], we will demonstrate this is not the main contributing factor to the difference in properties between these two regions.

3.2 Dielectric Properties

A high-throughput study of BSTO and BSTON dielectric properties as a function of composition was previously presented in Ref. [24] to which the reader is referred for further details. In this study, we consider only regions 1 and 2 for further TEM characterisation. Fig. 3 shows the ε_r and dielectric loss for BSTO films in regions 1 and 2 as a function of applied bias field from -300 kV to 300 kV, and frequencies from 1 kHz-100 kHz. ε_r, dielectric loss and tunability in Regions 1 and 2 have been extracted from Fig. 3 and listed in Table I. The tunability of the BSTO film is 63% and 50 % in Regions 1 and 2, respectively. As frequency

increases, a decrease in ε_r of the BSTO films was observed in both regions. The highest values for ε_r (636 and 321 for 0 and 300 kV/cm, respectively) were observed in region 2. However, the most significant difference between the dielectric properties of the two regions is the remarkably lower loss of the BSTO film in region 1 (Table I). ε_r and dielectric loss for region 2 at 100 kHz are not presented as they were too noisy due to the high conductivity.

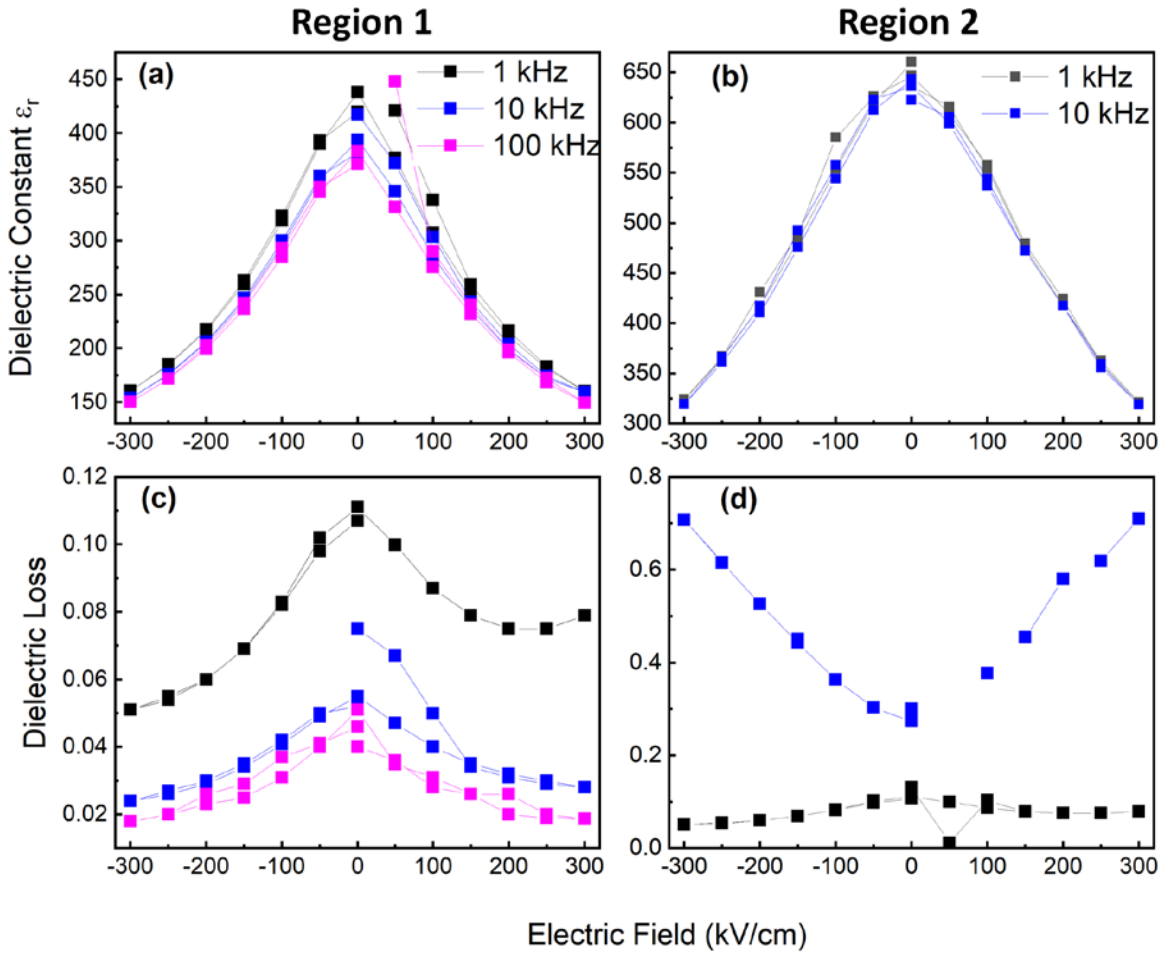

Figure 3: (a), (b) Dielectric constant and (c), (d) dielectric loss measured from the BSTO thin film at the region 1 (a, c) and region 2 (b, d) under the frequencies of 1, 10 and 100 kHz shown in blue, purple and green, respectively. The ac excitation voltage applied from the LCR Bridge was 100 mV.

Table I: Dielectric constant (ε_r), dielectric loss (tanδ) and tunability (n_r) calculated from Fig. 3 in 0 and 300 kV/cm electric fields at 1 and 10 kHz frequencies.

Frequency	Region	ε_r (0)	ε_r (300)	tanδ (0)	tanδ(300)	n_r (%)
1 kHz	Region 1	437	160	0.110	0.080	63.3
	Region 2	636	321	0.131	0.090	49.5
10 kHz	Region 1	417	159	0.075	0.028	61.8
	Region 2	623	319	0.300	0.710	48.7

3.2 TEM characterization

Fig. 4 shows STEM micrographs of cross sections of the BSTO thin films obtained from Regions 1 and 2. The thickness of the BSTO thin film is ~250 nm (Fig. 4) in both regions.

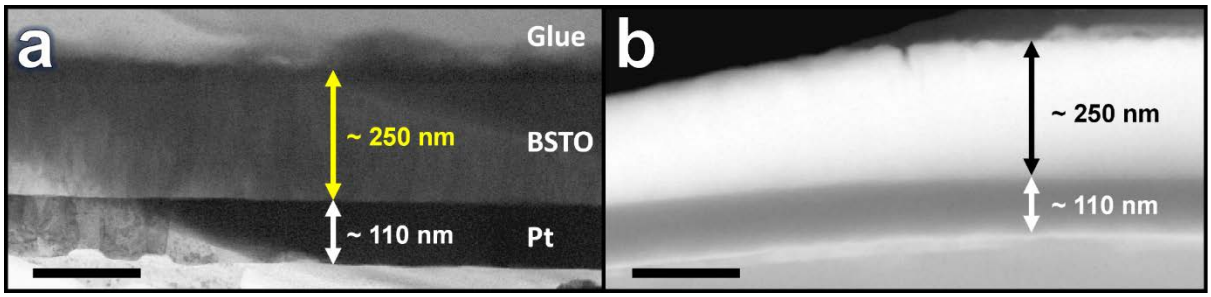

Figure 4: STEM images obtain from (a) region 1 (Bright Field) and (b) region 2 (Annular Dark Field) of the BSTO thin-film (scale bars are 200 nm).

No interfacial phases were observed between the BSTO and Pt in the (S)TEM images (e.g. Fig. 5(a-c)). In several cases, the grain boundary between adjacent BSTO grains (Fig. 5(a)) is coincident with the Pt grain boundary upon which they grow. Thus, the lateral size of the BSTO grains are governed by that of the Pt grains (50-100 nm) (Fig. 5(d)).

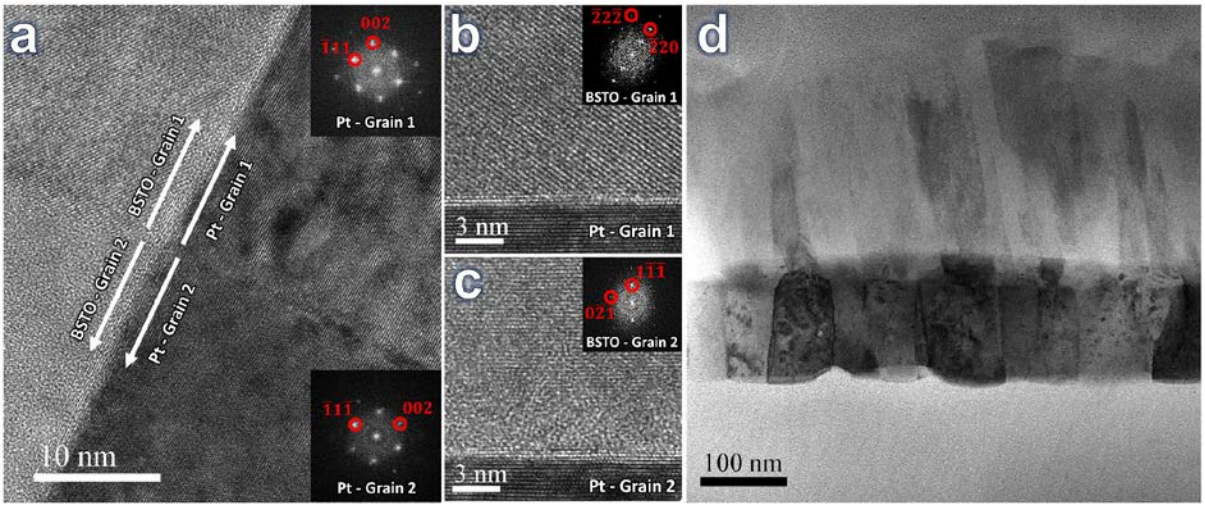

Figure 5: (a-c) HRTEM image obtained from BSTO-Pt interface in region 1; In this images Pt grains are close to [110] zone axis while BSTO grains are close to [110] (grain 1) and [312] (grain 2) zone axes. (d) BF-STEM image obtained from BSTO-Pt interface showing Pt has a lateral grain size of 50-100 nm.

EDX:

According to EDX analysis, the composition of the BSTO grains in each region is uniform across the film. (Fig. 6) The chemical compositions of the BSTO films extracted from EDX

spectra obtained from the Regions 1 and 2 are listed in Table II and have the approximate formulae, $Ba_{0.84}Sr_{0.16}TiO_{3\pm\delta}$ and $Ba_{0.83}Sr_{0.17}TiO_{3\pm\delta}$, respectively. These results indicate that there is only a small difference in the cation composition between these regions.

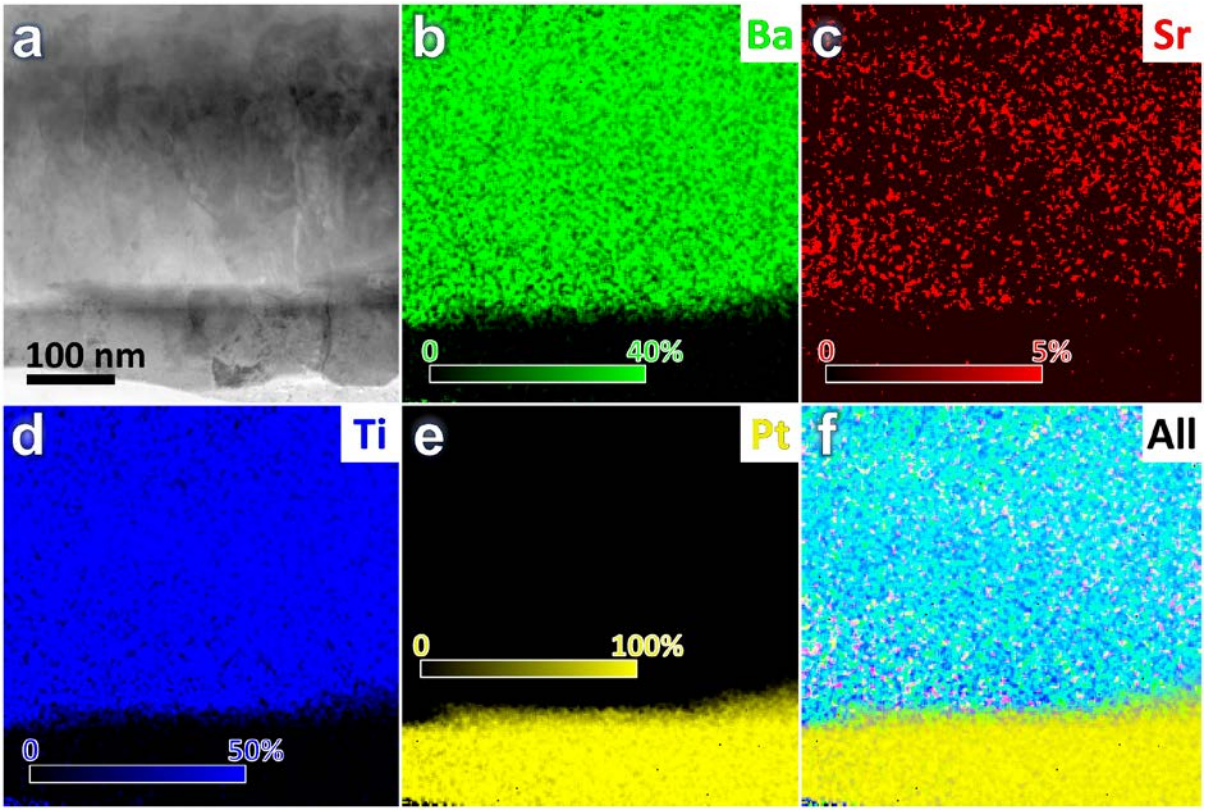

Figure 6: (a) BF-STEM image obtain from region 1. (b-f) EDX elemental maps corresponding to (a).

Table II. Chemical composition of the thin-films in Regions 1 and 2 extracted from EDX.

	Ba (at.%)*	**Sr (at.%)***	**Ti (at.%)***	**Composition**
Region 1	42.0 ± 0.9	8.0 ± 0.7	50 ± 1.0	$Ba_{0.84}Sr_{0.16}TiO_{3\pm\delta}$
Region 2	41.7 ± 0.9	8.3 ± 0.9	50 ± 1.0	$Ba_{0.83}Sr_{0.17}TiO_{3\pm\delta}$

* at.% values show the percentage of each cation among all cations.

EELS:

While the above EDX data provided the composition of the BSTO films, they did not reveal information regarding the bonding configurations and oxidation states of the ions. Analysis of bonding configurations in the BSTO films is feasible using the Ti-$L_{3,2}$ (~450 eV), Ba-$M_{5,4}$ (~780 eV), Sr-$L_{3,2}$ (~1940 eV) and O-K (~530 eV) edges. Electron transitions from $2p_{3/2}$ and $2p_{1/2}$ subshells of metallic Ti to unoccupied Ti-3d states form two white lines L_3 and L_2 in EELS, respectively. In Ti oxides, however, the coordination, site symmetry as well as valence

of the Ti atoms change the position and number of peaks in the Ti-$L_{3,2}$ white lines [29,30]. As Ti is in octahedral coordination with oxygen in BSTO, unoccupied Ti-3*d* orbitals split into a higher $3e_g$ (σ^*) molecular energy level and a lower $2t_{2g}$ (π^*) level [31]. Hence, as displayed in Fig. 7(a), Ti-L_3 and Ti-L_2 exhibit two white lines (i.e. π^* and σ^*) in the electron energy loss near-edge structure (ELNES) spectra obtained from the BSTO thin-films. Peak energies as well as intensity ratios of Ti-$L_{3,2}$ white lines extracted by fitting Lorentzian curves to the Ti-$L_{3,2}$ white lines are listed in Table III. The energies of the Ti white lines as well as π^* to σ^* energy ratios are in the same range for both Region 1 and 2, indicating that the average Ti valence is approximately the same.

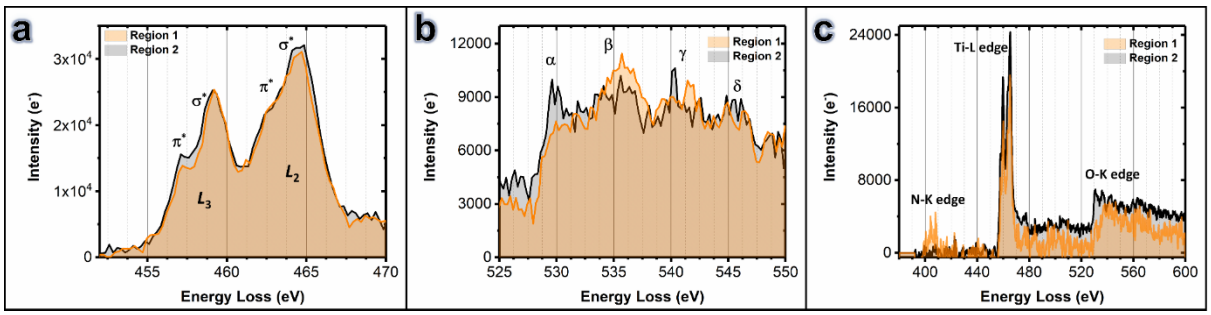

Figure 7: Experimental EELS data of the BSTO thin films showing (a) Ti $L_{3,2}$, (b) O *K* and (c) N *K* edges.

Table III. Ti ELNES energies (eV) and intensity ratios for the thin-films.

			Region 1	Region 2
Ti	L_3	E_{π^*}	457.12 ± 0.06	457.06 ± 0.06
		E_{σ^*}	459.14 ± 0.03	459.01 ± 0.04
	L_2	E_{π^*}	462.71 ± 0.09	462.67 ± 0.09
		E_{σ^*}	464.59 ± 0.05	464.63 ± 0.05
	I_{π^*}/I_{σ^*}		0.44 ± 0.07	0.39 ± 0.06

The O-*K* edge in BSTO thin-films (Fig. 7(b)) exhibits peaks due to hybridization of O-2*p* with Ti-3*d* (α), Sr-4*d* and Ba-5*d* (β) and high energy metal states, e.g. Sr-5*p*, Ba-6*p* and Ti-4*sp*, (γ and δ). As illustrated in Fig. 7(b), α has a relatively lower peak intensity in region 1. This is due to either the greater presence of V_{Ti}/V_O or to the greater substitution of N for O in the lattice in comparison with region 2. Our EDX and Ti-$L_{3,2}$ EELS results showed that Ti composition and its oxidation state are similar in region 1 and region 2; i.e. there is no significant difference in the V_{Ti}/V_O between these regions. However, a set of peaks at ~400 eV energy loss related to N-*K* edge (Fig. 7(c)) were obtained from region 1 that were absent from region 2, thereby

confirming that the decrease in the intensity of the α peak relates primarily to the substitution of N into the lattice.

IV. Discussion

Our (S)TEM results show that: i) the BSTO grains grow directly on the Pt substrate with no evidence of an interfacial layer; ii) the composition of the BSTO grains in each region is uniform; iii) the cation composition in both region 1 and region 2 is similar and iv) the oxidation state in each region is approximately the same. (Table II). Despite these similarities, region 1 has a higher tunability, lower relative permittivity and lower dielectric loss in comparison with region 2 (see Fig. 3 and Table I). Previous studies [20,21] have postulated there is a correlation between the dielectric degradation (higher conductivity loss) and the presence of V_O. The defect chemistry associated with the presence of V_O is summarised below using the Kroger Vink notation:

$$O_O^{\times} \rightarrow V_O^{\bullet\bullet} + \frac{1}{2}O_2(g) + 2e', \tag{3}$$

$$2e' + 2Ti_{Ti}^{\times} \rightarrow 2Ti_{Ti}', \tag{4}$$

V_O therefore, lead directly to the promotion of electrons to the conduction band and/or the associated formation of Ti^{3+} ions that facilitate a small polaron conduction mechanism [32,33]. However, the substitution of N for O in the lattice significantly alters the defect chemistry associated with titanates since:

$$N_2(g) + 3O_O^{\times} \rightarrow 2N_O' + V_O^{\bullet\bullet} + \frac{3}{2}O_2(g). \tag{5}$$

The substitution of N for O, Eq. (5), therefore compensates for the formation of Ti^{3+}, Eq. (3), and limits the promotion of electrons to the conduction band or inhibits small polaron hopping, Eq. (4), depending on the conduction mechanism within the film. This has direct implications for the dielectric properties; the dielectric loss is dramatically improved, the contribution to relative permittivity from space charge polarisation is suppressed and tunability relating to the polarisation of the perovskite lattice is enhanced. The presence of N in Region 1 therefore, may be used to explain the superior properties observed in this region. However, Region 2 has undergone an identical treatment in N_2 and has little or no difference in composition or microstructure. The question remains therefore, why region 2 has not undergone substitution of N for O in the lattice when the evidence is overwhelming for this

effect in region 1. Pertinently, EELS analysis of other regions near the edge of the sample also revealed that N had not substituted for O.

We note that the samples are placed in a tube furnace and heat treated in flowing N_2 at 650 ^oC. The tube furnace diameter is approximately 2x that of the sample width and hence all of the sample is within a region of lamellar rather than turbulent N_2 flow. Moreover, the sample is fully within the hot zone of the furnace. Thus, within the experimental set-up there is no difference in the temperature or concentration of N_2 in the furnace atmosphere.

The most likely explanation, however, relates to the thin region of exposed Pt around the edge of the sample (see Fig. 1(a)). We speculate that O atoms are absorbed/adsorbed by Pt [34,35] during the deposition of the BSTO films in the MBE chamber and are released on reheating in the N_2 atmosphere. The local $P(N_2)$ at the edge of the film is affected by the evolution of O from the Pt, inhibiting substitution of N for O.

V. Conclusions

BSTO thin-films with a thickness of ~170-250 nm were successfully deposited on Pt(111) by high throughput evaporative physical vapour deposition (HT-ePVD). We have investigated the structure and chemistry of two samples of BSTO thin-films, with different dielectric properties using (S)TEM. We find direct evidence, using EELS, for N substituting for O in the lattice of BSTO. BSTO film regions containing higher N concentration exhibit lower dielectric loss (0.04 under zero field) and higher dielectric tunability (63.3%) in comparison to the film containing low (no) N concentration (dielectric loss of 0.131 under zero field and tunability of 49.5%). We propose than N compensates for Ti^{3+} ions, thereby suppressing conductivity, decreasing dielectric loss and enhancing tunability.

Acknowledgements

The authors acknowledge the Engineering and Physical Sciences Research Council (EPSRC) grants EP/N032470/1, EP/N032233/1 and the Henry Royce Institute for Advanced Materials, funded through EPSRC grants EP/R00661X/1 for JEOL JEM-F200 access at Royce@Sheffield.

References

[1] S. Ito, H. Funakubo, I.P. Koutsaroff, M. Zelner, A. Cervin-Lawry, Applied Physics Letters **90**, 142910 (2007).
[2] A. Tombak, J.P. Maria, F. Ayguavives, Z. Jin, G.T. Stauf, A.I. Kingon, A. Mortazawi, Ieee Microwave and Wireless Components Letters **12**, 3 (2002).
[3] P. Bao, T.J. Jackson, X. Wang, M.J. Lancaster, Journal of Physics D-Applied Physics **41**, 063001 (2008).
[4] M. Jain, S.B. Majumder, R.S. Katiyar, A.S. Bhalla, Materials Letters **57**, 4232 (2003).
[5] H. Bouyanfif, J. Wolfman, M. El Marssi, Y. Yuzyuk, R. Bodeux, M. Gervais, F. Gervais, Journal of Applied Physics **106**, 034108 (2009).
[6] A. Tombak, F.T. Ayguavives, J.P. Maria, G.T. Stauf, A.I. Kingon, A. Mortazawi, *Low Voltage Tunable Barium Strontium Titanate Thin Film Capacitors for RF and Microwave Applications*, in: T. Perkins (Ed.) 2000 Ieee Mtt-S International Microwave Symposium Digest, Vols 1-32000, pp. 1345.
[7] C. Basceri, S.K. Streiffer, A.I. Kingon, R. Waser, Journal of Applied Physics **82**, 2497 (1997).
[8] T. Hayashi, N. Oji, H. Maiwa, Japanese Journal of Applied Physics **33**, 5277 (1994).
[9] G. Arlt, D. Hennings, G.d. With, Journal of Applied Physics **58**, 1619 (1985).
[10] Y. Tan, J. Zhang, Y. Wu, C. Wang, V. Koval, B. Shi, H. Ye, R. McKinnon, G. Viola, H. Yan, Scientific Reports **5**, 9953 (2015).
[11] Z. Zhao, V. Buscaglia, M. Viviani, M.T. Buscaglia, L. Mitoseriu, A. Testino, M. Nygren, M. Johnsson, P. Nanni, Physical Review B **70**, 024107 (2004).
[12] C. Rayssi, S. El.Kossi, J. Dhahri, K. Khirouni, RSC Advances **8**, 17139 (2018).
[13] J. Gao, Y. Liu, Y. Wang, X. Hu, W. Yan, X. Ke, L. Zhong, Y. He, X. Ren, The Journal of Physical Chemistry C **121**, 13106 (2017).
[14] E. Ertekin, V. Srinivasan, J. Ravichandran, P.B. Rossen, W. Siemons, A. Majumdar, R. Ramesh, J.C. Grossman, Physical Review B **85**, 195460 (2012).
[15] X.H. Zhu, D.N. Zheng, W. Peng, A. Li, Y.F. Chen, *Enhanced Dielectric Properties of Mn Doped $Ba_{0.6}Sr_{0.4}TiO_3$ Thin Films Fabricated by Pulsed Laser Deposition*, 2006.
[16] O.G. Vendik, S.P. Zubko, Journal of Applied Physics **88**, 5343 (2000).
[17] H.J. Cho, H.J. Kim, Applied Physics Letters **72**, 786 (1998).
[18] G.A. Boni, C.F. Chirila, L. Hrib, R. Negrea, L.D. Filip, I. Pintilie, L. Pintilie, Scientific Reports **9**, 14698 (2019).
[19] J. George, J. Beeckman, W. Woestenborghs, P. Smet, W. Bogaerts, K. Neyts, Nanoscale research letters **8**, 62 (2013).
[20] T. Baiatu, R. Waser, K.H. Hardtl, Journal of the American Ceramic Society **73**, 1663 (1990).
[21] S.J. Lee, S.E. Moon, H.C. Ryu, M.H. Kwak, Y.T. Kim, Japanese Journal of Applied Physics Part 1-Regular Papers Short Notes & Review Papers **41**, 4597 (2002).
[22] S. Guerin, B.E. Hayden, Journal of Combinatorial Chemistry **8**, 66 (2006).
[23] I. Bakaimi, X. He, S. Guerin, N.Z.I. Hashim, Q. Luo, I.M. Reaney, S. Gao, B.E. Hayden, C.H.K. de Groot, Journal of Materials Chemistry C **6**, 6222 (2018).
[24] A. David, S. Guérin, B.E. Hayden, R. Noble, J.-P. Soulié, C. Vian, I.P. Koutsaroff, S.i. Higai, N. Tanaka, T. Konoike, A. Ando, H. Takagi, T. Yamamoto, T. Fukura, H. Ieki, Crystal Growth & Design **14**, 523 (2014).
[25] S. Guerin, B.E. Hayden, Chemical Communications **55**, 10047 (2019).
[26] M. Zhang, C. Deng, Ceramics International **45**, 22716 (2019).
[27] J. Lyu, I. Fina, R. Solanas, J. Fontcuberta, F. Sánchez, Scientific Reports **8**, 495 (2018).

[28] W. Zhang, H. Cheng, Q. Yang, F. Hu, J. Ouyang, Ceramics International **42**, 4400 (2016).
[29] E. Stoyanov, F. Langenhorst, G. Steinle-Neumann, American Mineralogist **92**, 577 (2007).
[30] A. Mostaed, G. Balakrishnan, M.R. Lees, Y. Yasui, L.J. Chang, R. Beanland, Physical Review B **95**, 094431 (2017).
[31] L.A. Grunes, R.D. Leapman, C.N. Wilker, R. Hoffmann, A.B. Kunz, Physical Review B **25**, 7157 (1982).
[32] M. Reticcioli, U. Diebold, G. Kresse, C. Franchini, *Small Polarons in Transition Metal Oxides*, in: W. Andreoni, S. Yip (Eds.) Handbook of Materials Modeling: Applications: Current and Emerging Materials, Springer International Publishing, Cham, 2019, pp. 1.
[33] M. Setvin, C. Franchini, X. Hao, M. Schmid, A. Janotti, M. Kaltak, C.G. Van de Walle, G. Kresse, U. Diebold, Physical Review Letters **113**, 086402 (2014).
[34] Z.H. Gu, P.B. Balbuena, Journal of Physical Chemistry C **111**, 9877 (2007).
[35] R. Lewis, R. Gomer, Surface Science **12**, 157 (1968).